Biomedical Engineering: Applications, Basis and Communications, Vol. 26, No. 1 (2014) 1450012 (21 pages)
DOI: 10.4015/S1016237214500124

World Scientific
www.worldscientific.com

MODELING HUMAN TISSUES: AN EFFICIENT INTEGRATED METHODOLOGY

M. Cerrolaza[*,§], G. Gavidia[†], E. Soudah[*] and M. Martín-Landrove[‡]
[*]*International Center for Numerical Methods in Engineering*
Polytechnic University of Catalonia, Barcelona, Spain
[†]*Biomedical Engineering Research Center*
Polytechnic University of Catalonia, Barcelona, Spain
[‡]*National Institute of Bioengineering*
Central University of Venezuela, Caracas, Venezuela
[§]*mcerrolaza@cimne.upc.edu*

Accepted 7 April 2013
Published 26 February 2014

Biomed. Eng. Appl. Basis Commun. 2014.26. Downloaded from www.worldscientific.com
by Eduardo Soudah on 02/18/15. For personal use only.

ABSTRACT

Geometric models of human body organs are obtained from imaging techniques like computed tomography (CT) and magnetic resonance image (MRI) that oallow an accurate visualization of the inner body, thus providing relevant information about their its structure and pathologies. Next, these models are used to generate surface and volumetric meshes, which can be used further for visualization, measurement, biomechanical simulation, rapid prototyping and prosthesis design. However, going from geometric models to numerical models is not an easy task, being necessary to apply image-processing techniques to solve the complexity of human tissues and to get more simplified geometric models, thus reducing the complexity of the subsequent numerical analysis. In this work, an integrated and efficient methodology to obtain models of soft tissues like gray and white matter of brain and hard tissues like jaw and spine bones is proposed. The methodology is based on image-processing algorithms chosen according to some characteristics of the tissue: type, intensity profiles and boundaries quality. First, low-quality images are improved by using enhancement algorithms to reduce image noise and to increase structures contrast. Then, hybrid segmentation for tissue identification is applied through a multi-stage approach. Finally, the obtained models are resampled and exported in formats readable by computer aided design (CAD) tools. In CAD environments, this data is used to generate discrete models using finite element methed (FEM) or other numerical methods like the boundary element method (BEM). Results have shown that the proposed methodology is useful and versatile to obtain accurate geometric models that can be used in several clinical cases to obtain relevant quantitative and qualitative information.

Keywords: 3D modeling; Human tissues; Segmentation; Medical images; Finite element method.

INTRODUCTION

Geometric models of human body parts, such as organs and tissues, as well as their pathologies, planning and surgery are usually carried out by using numerical methods to get approximate models of such organs. To obtain a tissue model using numerical methods, such as the finite element method (FEM), the geometric model of the organ is divided into surface or volumetric elements, the properties of each element are formulated, and then the elements are combined to compute the organ's deformation states under the influence of external forces applied by surgical instruments.[1] However,

[§]Corresponding author: M. Cerrolaza, International Center for Numerical Methods in Engineering, Polytechnic University of Catalonia, Barcelona, Spain. Tel:+34 93 4134167, +34 660 702061; Fax: +34 93 4016035; E-mail:mcerrolaza@cimne.upc.edu

Biomed. Eng. Appl. Basis Commun. 2014.26. Downloaded from www.worldscientific.com by Eduardo Soudah on 02/18/15. For personal use only.

the generation of these models is not a trivial task, considering the complex shape of human anatomic parts, which are generally not symmetric. Likewise, the imposition of boundary conditions and biological loadings in the model are neither trivial nor simple tasks. Actually, soft tissues such as brain or heart and hard tissues such as bone have a diverse and complex morphology, usually overlapping. Current techniques such as magnetic resonance (MR), computed tomography (CT) and positrons emission tomography (PET) have been used, among others, based on radiations which produce images when interacting with human tissues. The reconstruction of human tissues is carried out with digital processing techniques. A gray-scale medical image is represented by a $m \times n \times z$ matrix, formed by several parallel slices of images in the z direction, having $m \times n$ pixels. Each matrix element has a gray-intensity value obtained by the interaction between radiation and human tissue. Processing and visualization techniques for medical images involve a set of mathematical algorithms, applied to the matrix representation described above in order to modify their elements values. There exist some previous works on this subject[2–4] that have studied the process to extract and to analyze human anatomic structures from these radiological techniques. The aforementioned authors agree to define three main steps, once the medical data have been digitalized: (a) images preprocessing to reduce noise and enhance contrast, (b) segmentation to extract regions of interest for further analysis and (c) visualization of segmented regions (volume, surfaces, discretized meshes) for further manipulation.

These studies, based on the manipulation and visualization of medical images, are a key aspect for medical diagnosis and diseases treatment. These techniques not only allow medical doctors and scientists to obtain vital information by using non-invasive techniques but also they are essential tools in getting more accurate geometric models of human body parts. Some works on this research line can be mentioned here. 3D models of highly heterogeneous bone from CT images have been obtained in Ref. 5. The authors then used the FEM for the mechanical analysis of bone. In Ref. 6, a new methodology to get titanium-prostheses designs from CT bone-structures has been proposed. These authors applied processing techniques for images and modeling using the FEM. Isaza *et al.*[7] reconstructed facial-skull structures from CT images by applying image processing techniques to get the segmentation of structures of interest. Then they applied the FEM to simulate a device used in orthodontics, both for the dental and skeletal use in cervical traction.

The main goal of this work is to propose an integrated methodology to obtain geometric models of human-body parts, which will help in medical visualization, measurement, biomechanical simulation, rapid prototyping and prosthesis design.

IMAGE PROCESSING AND VISUALIZATION

Medical imaging provides major aid in many branches of medicine: it enables and facilitates the capture, transmission and analysis of medical images as well as provides assistance for medical diagnoses. Medical imaging is still on the rise with new imaging modalities being added and continuous improvements of devices' capabilities. Preprocessing, segmentation and contour extraction are important steps in tissue models generation. Preprocessing is necessary because biomedical images are often corrupted by noise and sampling artifacts, which can cause considerable problems when applying rigid methods. Segmented images and contour extraction are used to obtain anatomical structures and they are commonly used in a wide variety of applications: diagnosis, preoperative planning, pathology localization and computer-integrated surgery. However, preprocessing and image segmentation remain a difficult task due to both the variability of object shapes and image quality. Medical images frequently display high-intensity variations throughout the regions that correspond to the same tissue type. Also, two different tissues can share very similar intensity profiles.

Preprocessing and segmentation using traditional low-level image processing techniques such as thresholding, histogram, convolution and other classical operations, require a considerable amount of interactive guidance in order to get satisfactory results. Automating these model-free approaches is diffcult because of shape complexity, shadows and variability within and across individual objects. Noise and other image artifacts can cause incorrect regions or boundary discontinuities in objects recovered from these methods. For these reasons, it is accepted that despite the more complex algorithms developed so far, the preprocessing and segmentation of medical images remain highly dependent on the image modality and the type of tissue under study.

In this work, the main methods commonly used in medical images are explored. Finally the proposed methodology is applied to several hard and soft tissues including jaw, spine, skull and brain.

Biomed. Eng. Appl. Basis Commun. 2014.26. Downloaded from www.worldscientific.com
by Eduardo Soudah on 02/18/15. For personal use only.

Main Problems and Characteristics of Medical Images

Medical images are usually contaminated by noise generated by interference or other sources. Usually, noise is inherent to the medical images acquisition and to the performance of medical instruments as well.[4] Moreover, radiological procedures modify the image contrast and visualization details.[2] Thus, it is mandatory to modify the gray-intensity range of images in order to improve the visualization of more brilliant zones as compared to other not so brilliant ones. The success in getting reliable tissue geometric-models will depend on the techniques used in this first step.

Noise in image space

Image noise is usually characterized by the distribution and amplitude values and their levels vary according to the tissue and to the spatial resolution of each image. In medical images, the noise is due to stochastic processes in image acquisition or during their reconstruction. To address this problem, some reduction filters (to be used further as shown in Figs. 8, 12 and 14) have been developed using Gauss distribution. An image corrupted by noise can be described as follows:

$$v(x,y) = g[u(x,y)] + n(x,y), \tag{1}$$

$$g[u(x,y)] = \iint n(x,y,x',y')u(x',y')dx'dy', \tag{2}$$

where $u(x,y)$ is the original image and $v(x,y)$ is the observed image (corrupted by noise); $n(x,y)$ stands for the additive noise. The formation image process can be modeled by the linear system described in Eq. (1), where $n(x,y,x',y')$ is the response to the image acquisition.

The interpretation of noise in a medical image will depend on the image itself and on the visual perception. The estimation of the statistical characteristics of noise in an image is needed to separate the noise from the image. Four kinds of noise are usually reported (see Ref. 9): additive, multiplicative, impulsive and quantification noise. Since additive and multiplicative are the most commonly observed noises in medical images, we include a brief description below:

- *Additive noise.* This is generated by white Gaussian sensors, as defined in Eq. (3), where $g(x,y)$ is the observed image having noise resulting from the image $I(x,y)$ corrupted by additive noise $n(x,y)$

$$g(x,y) = I(x,y) + n(x,y). \tag{3}$$

Figure 1 shows an example of additive noise, resulting from adding Gaussian-type noise to a phantom image which simulates a MRI of brain. The behavior of added noise can be observed in the histogram shown in Fig. 1(D).

- *Multiplicative noise.* This is a kind of speckle noise, observed in medical images, particularly in ultrasound and MRI. This kind of noise is represented in Eq. (4), where $g(x,y)$ is the observed image having noise, $I(x,y)$ is the image in formation, $c(x,y)$ is the multiplicative noise component and $n(x,y)$ is the added noise.

$$g(x,y) = I(x,y)c(x,y) + n(x,y). \tag{4}$$

Figure 2 shows an example of multiplicative noise added to a phantom image that represents a MR brain

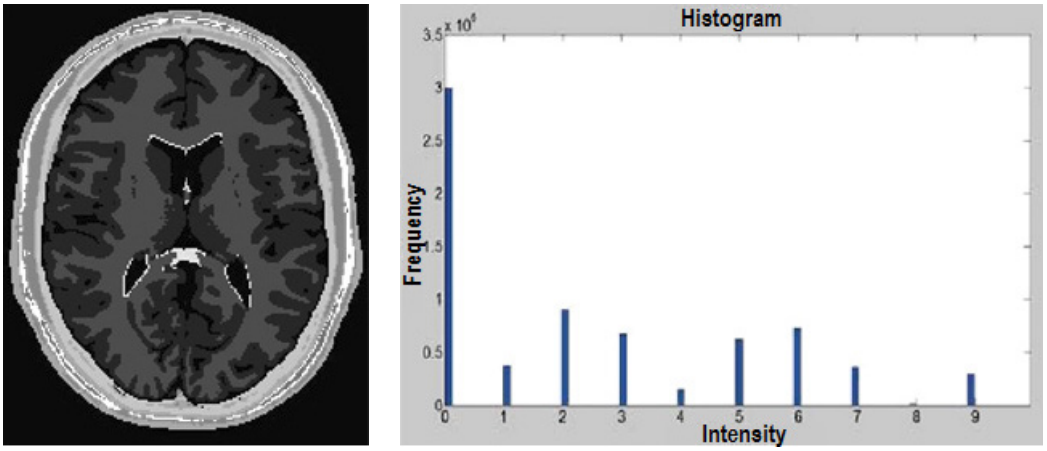

(A) **(B)**

Fig. 1 Brain phantom corrupted by additive noise. **(A)** Axial slice of original phantom. **(B)** Histogram of A. **(C)** Original image in A with Gaussian additive noise. **(D)** Histogram of C.

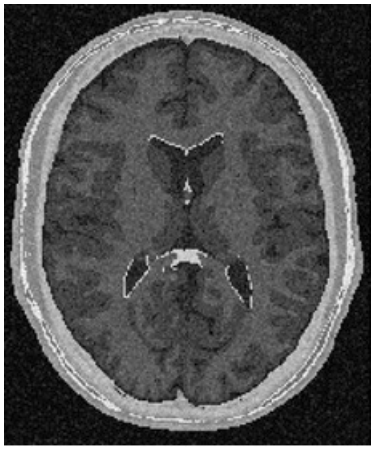

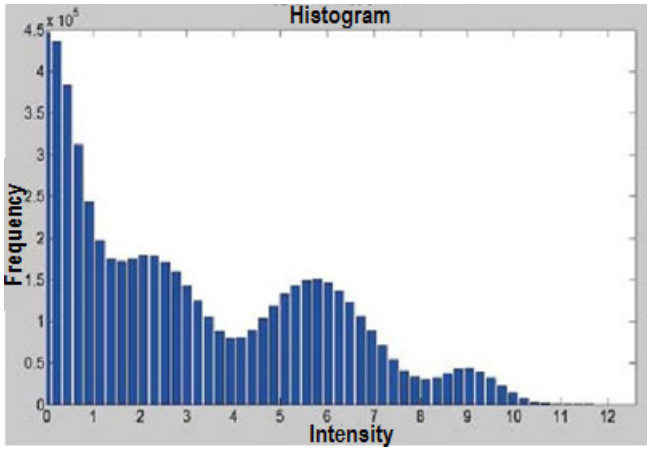

(C) (D)

Fig. 1 (*Continued*)

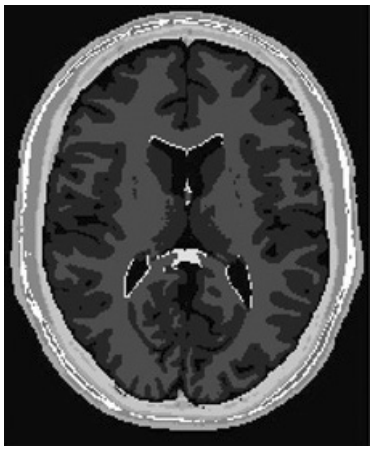

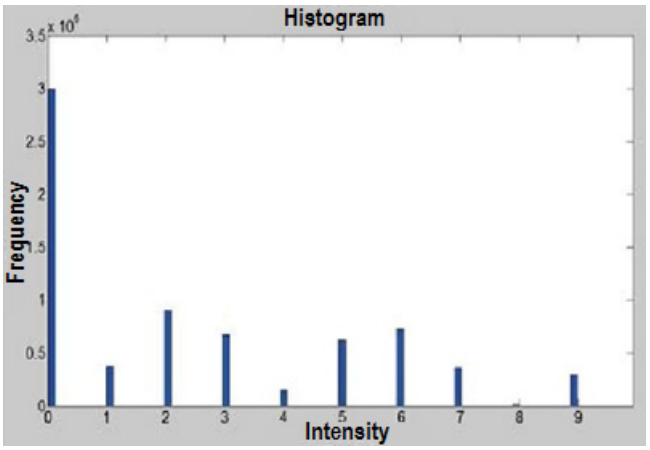

(A) (B)

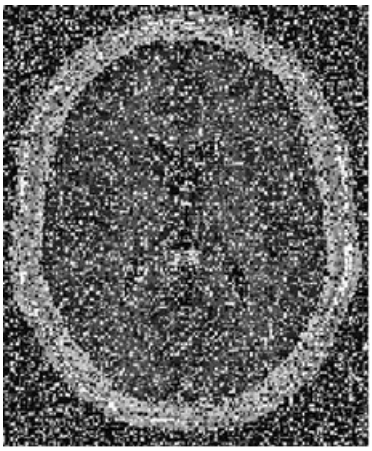

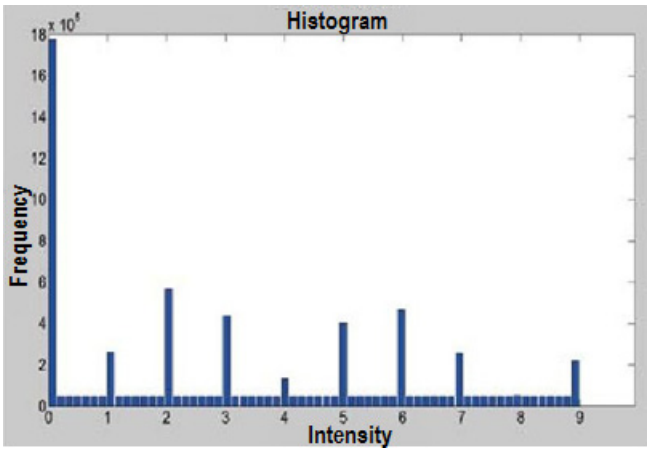

(C) (D)

Fig. 2 Brain phantom corrupted by multiplicative noise: **(A)** Axial slice of original phantom. **(B)** Histogram of A. **(C)** Original image corrupted by multiplicative noise. **(D)** Histogram of C.

Biomed. Eng. Appl. Basis Commun. 2014.26. Downloaded from www.worldscientific.com
by Eduardo Soudah on 02/18/15. For personal use only.

Biomed. Eng. Appl. Basis Commun. 2014.26. Downloaded from www.worldscientific.com
by Eduardo Soudah on 02/18/15. For personal use only.

image. For the sake of simplicity, $c(x, y)$ was assumed constant in Fig. 2. The noise behavior can be observed in Fig. 2(D).

Edge and discontinuous zones between tissues

The edge is defined as an abrupt increase in the intensity values which shows the boundaries, or separation lines, among the different objects in it. In the image the objects boundaries are seen as discontinuities of certain properties such as intensity, color and texture. In medical images, tissues are separated by edges and discontinuous zones that are detected through diverse techniques. However, a zone of interest may not be necessarily detected without further processing. In the present study, the image-gradient technique was used to enhance medical-image edges, previously smoothed using the anisotropic diffusion filter. When these filters are applied on a gray-scale image, they calculate the image gradient (∇I) at each point (pixel or voxel) providing the direction of the largest possible increase (black or white). The gradient of the image "I" at a point in the directions X, Y, Z is computed by Eq. (5).

$$\nabla I = \left[\frac{\partial I}{\partial x}, \frac{\partial I}{\partial y}, \frac{\partial I}{\partial z}\right]. \tag{5}$$

The final results show how abrupt or soft the image changes at each point are. It also shows how a specific point represents an image edge and its orientation. Figure 3 depicts a facial-skull CT image with the boundaries highlighted through the gradient calculation in directions X, Y, Z. Note that Eq. (5) can also be used in MRI.

Segmentation of Images into Contiguous Regions

Once the intensity levels are improved and medical images devices are corrected, the next stage is segmentation, which consists in dividing images into contiguous regions (sub-regions or sub-volumes) whose elements (pixels or voxels) have common cohesion properties. A previous step is to extract the quantitative and qualitative parameters and evaluate the morphology and functioning of the segmented object. Success depends on an optimal pre-processing.

The segmentation algorithms of medical images play an important role in medical diagnosis and treatment. These are used in anatomic structures analysis, type of tissue, spatial distribution function and organs activity and pathological regions. Its application includes brain tumor detection,[10] extraction of an area affected by extra-pulmonary tuberculosis,[11] heart pathologies visualization,[12] coronary borders in angiograms, multiple sclerosis damage quantification, surgery planning and simulation, tumor volume measuring and tumor response to therapies, blood cells automated classification, brain development study, micro calcifications in mammographies among other applications.

The methods used to carry out the segmentation process vary according to the specific need, image type, among other factors. For example, the brain tissue segmentation is different from the heart or bone segmentation, such as a jaw or femur. It has been found that specialized methods for specific applications can lead to better results when having a prior knowledge. However, the choice of the right method for segmentation problems, when dealing with all types of medical images, is sometimes diffcult due to the lack of robust methods. We

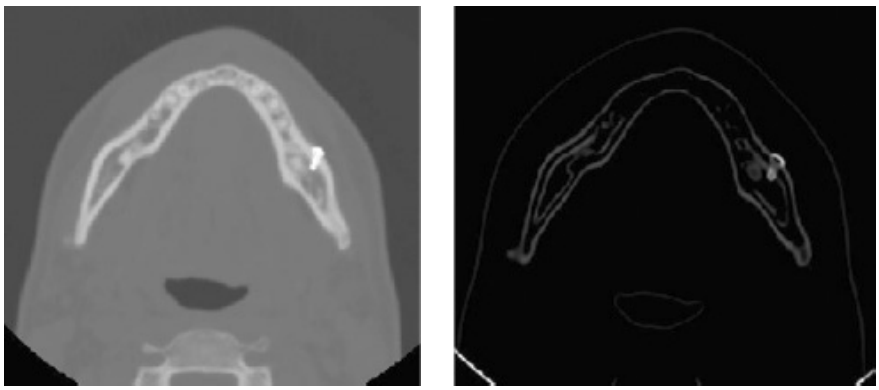

(A) **(B)**

Fig. 3 Craneofacial CT image with highlighted boundaries: **(A)** Original CT image. **(B)** Boundaries detection in A with the gradient size calculation in directions X, Y, Z.

have combined several segmentation methods which is known as the hybrid segmentation approach.

Manual segmentation vs. automated segmentation

The performance of image segmentation approaches is nowadays a persistent challenge. Manual segmentation based on interactive drawing of the desired segmentation by domain experts is often the only acceptable approach and yet suffers from intraexpert and interexpert variability. Automated image segmentation algorithms have been sought in order to remove the variability introduced by experts. The balance between manual interaction and performance is an important consideration in any segmentation application while manual interaction can improve accuracy by incorporating prior knowledge of an operator. Nevertheless, for large population studies, this can be laborious and time consuming. The type of interaction required by segmentation methods can range from completely manual delineation of an anatomical structure to the selection of a seed point for a region growing algorithm (see Sec. 3.3.1). The differences in these types of interactions are the amount of time and effort required, as well as the amount of training required by the operator. Methods that rely on manual interaction can also be vulnerable to reliability issues. However, even "automated" segmentation methods typically require some interaction for specifying initial parameters that can significantly affect performance.

Validation of segmented volumes

The accuracy of segmentation method of medical images has been difficult to quantify in the absence of a "ground truth" segmentation for clinical data. Validation is typically performed using one of two different types of truth models. The most straightforward approach to validation is by comparing the volumes obtained by automated segmentation with volumes obtained by manual segmentation. This approach, besides suffering from the drawbacks outlined in the previous section, does not guarantee a perfect truth model since an operator's performance can also be flawed. The other common approach for validating segmentation methods is the use of physical phantoms or computational phantoms. Physical phantoms provide an accurate depiction of the image acquisition process but typically do not present a realistic representation of anatomy. Computational phantoms can be more realistic in this latter regard, but simulate the image acquisition process using only simplified models. Although digital or computational phantoms can provide a level of known "ground truth", it has so far been unable to reproduce the full range of imaging characteristics (partial volume artifact, intensity inhomogeneity artifact, noise) and normal and abnormal anatomical variability observed in clinical data.[13] A common alternative to phantom studies has been a behavioral comparison of algorithms: an automated algorithm is compared to the segmentations generated by a group of experts and, if the algorithm generates segmentations suffciently similar to the experts, it is regarded as an acceptable substitute for the experts. Typically, good automated segmentation algorithms will also require less time to apply, having better reproducibility than interactive segmentation by an expert.

Tissue Visualization

3D visualization of tissues strongly depends on computational tools which make easier the human–machine interaction when dealing with hard and soft tissues exploration and analysis. From the engineering point of view, these aspects pose a challenge because functional characteristics must be displayed in different visual forms to help the interpretation of multi-dimensional information and the correlation of qualitative and quantitative information at the same time. Another critical issue is to guarantee the 3D perspective realism for the spatial representation of the data, temporal information representation and other visual signals such as textures and tones as well as solving the interaction model between users and the information through visualization systems. Modeling is a breakthrough in biomedical research by making analytical formulations to describe physiological functions. Nowadays, a new approach has been assumed by biomedical and mechanical engineers to tackle the modeling problems based on visualization because it allows the validation of the qualitative model. Likewise, the visualization techniques required now for modeling applications and biomedical simulation should cover multidisciplinary areas such as the finite element modeling and computational fluid dynamics among others. This should help in getting faster the prototypes and their parameters.

3D visualization refers to a visual representation obtained through a set of slices of the same resolution, aligned parallel with respect to an adjacent position (z-coordinate) obtaining a volume consisting of voxels.[14] The birth of medical images based on 3D information such as MR, CT, PET, among others, set the beginning of diverse research studies in 3D medical images reconstruction to obtain a volumetric view of soft tissues[15–18] and hard tissues.[5–7,19]

Biomed. Eng. Appl. Basis Commun. 2014.26. Downloaded from www.worldscientific.com by Eduardo Soudah on 02/18/15. For personal use only.

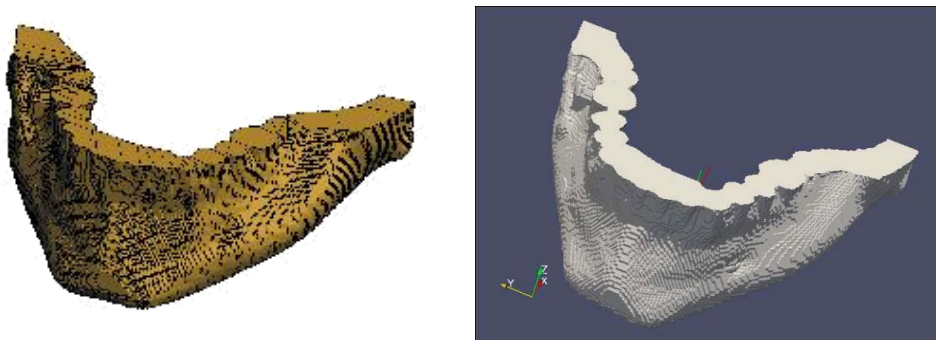

(A) **(B)**

Fig. 4 3D reconstruction of a jaw bone: **(A)** Volumetric view **(B)** isosurfaces view.

Biomed. Eng. Appl. Basis Commun. 2014.26. Downloaded from www.worldscientific.com by Eduardo Soudah on 02/18/15. For personal use only.

The 3D visualization of human-body parts from medical image reconstruction is an advantage for medical doctors as it adds a third dimension to the views displayed on the computer providing a more complete information. However, one of the main problems in 3D representation is how users can interpret and manipulate the information in a faster way. Thus, it is advisable to use specific visualization routines that focus on areas of interest and showing the results in a faster and more reliable way. Another aspect to take into consideration is the computational cost of 3D visualization systems, which tends to be high because of the amount of data.

One approach to reduce the high computational cost involved in 3D visualization of biological structures was presented in Ref. 20, in which isosurfaces were extracted from volumes obtained through CT. An isosurface is a visual representation of a structure obtained through a voxel, which has the same or similar intensity value. This technique is also known as 3D boundary extensions, 3D boundaries or sometimes boundary surfaces.[3] The main idea is to extract a surface from a volume of 3D data as a collection of adjacent polygons and visualizing the extracted surfaces with appropriate algorithms.[14] With this technique it is possible to display, manipulate and extract geometric information from structures in a faster way. One of the best known isosurfaces extracting algorithms from volumetric data is the Marching Cubes Algorithm proposed in Ref. 21. The authors examined each basic element (volume cell) and generated a triangulation over it. In Fig. 4(B) a jaw bone surface obtained from a 3D volume [Fig. 4(A)] is shown.

PROPOSED METHODOLOGY

To obtain useful geometric tissue models it is necessary to properly apply a set of image-processing techniques to deal with the complexity of human tissues and to get simplified models. These models will reduce the complexity of the subsequent numerical analysis. In this way, the geometric models obtained by this methodology will be used to generate surface and complex finite element meshes, which will help in visualization, measurement, biomechanical simulation, rapid prototyping and prosthesis design. Thus we propose an integrated methodology based in the observation of tissue type, its intensity profiles and its boundary quality, which consists of five main steps integrated into the computational tool biomedical view.[22,23] The algorithms were developed using MATLAB tool[8] and the Insight ToolKit (ITK) library code.[24] The flowchart of the proposed methodology is shown in Fig. 5.

The first step of the methodology, called 3D reconstruction, leads to an initial volume from 2D medical images. The second step consists in to apply preprocessing techniques to the original volumes in order to reduce noise and other artifacts. These techniques are chosen according to the image characteristics.

The third step is the segmentation of the initial volume considering regions-of-interest (ROI) such as soft and hard tissues. The fourth step refines the obtained models by applied morphological operators and gaussian filter. Finally, in the last step, the volumes are saved in standard output format readable by the most of CAD programs or the geometric model discretization through numerical methods. Each one of the steps of the methodology are explained in detail in the following sections.

Step 1: Reading Images and 3D Reconstruction

The initial 3D reconstruction of Digital Imaging and Communication in Medicine (DICOM) images was done by parallel stacking of each slice with respect to the Z axis. The next step was to select a ROI in the initial 3D image to obtain sub-volumes containing zones of

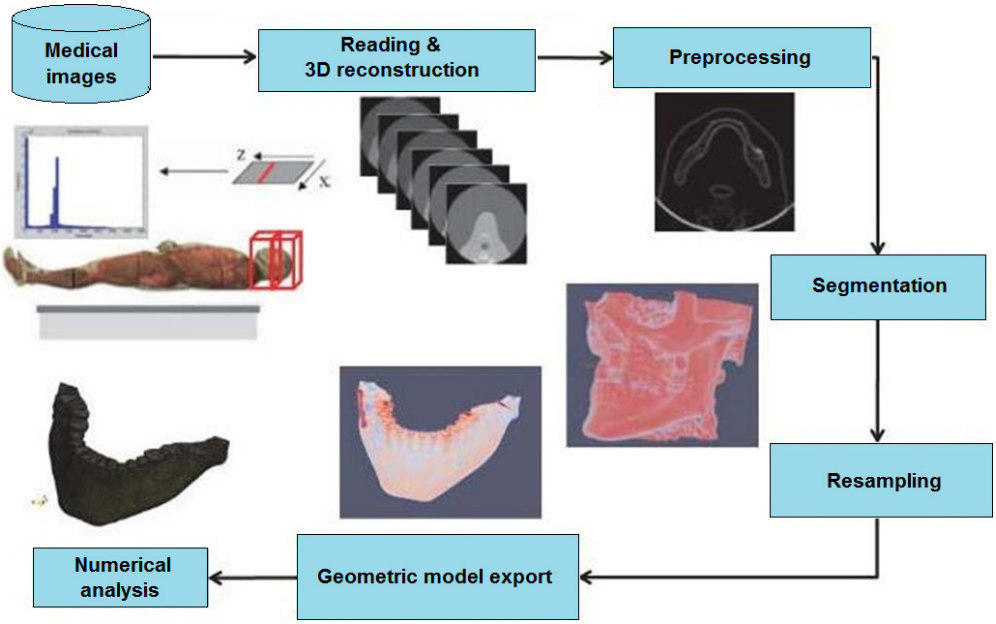

Fig. 5 Schematic flowchart of integrated methodology.

interest. In each one of the sub-volumes a flowchart consisting of algorithms was applied from the preprocessing step to obtain the relevant tissue-volume.

Step 2: Preprocessing

Noise and artifact reduction in image space

For image noise elimination, the gradient anisotropic diffusion filter of ITK was used to implement a N-dimensional version of the classic equation of anisotropic diffusion proposed by Preona and Malik.[25] (see Eq. (6)). In this equation, an edge detector $|\nabla I|$ is used, which is responsible for noise smoothing and whose value becomes infinite when approaching a perfect edge

$$I_t = \nabla \cdot (g(|\nabla I|)\nabla I). \tag{6}$$

The function $|\nabla I|$ is used to reduce conductance in high value areas. $|\nabla I| = 0$ where the gradient is high and decreases completely in low gradients. It means $g(x) \to 0$, if $x \to \infty$ (reached value in one edge) and $g(x) \to 1$, if $x \to 0$ (reached value within a region).

Edge enhacement in regions of interest

Different tissues or ROI can be visualized in the images and it may be hard to separate from each other. The solution is to calculate the gradient image and its module, which is useful to determine the boundaries and the separation of the left ventricle from the right ventricle and the descending aorta. The gradient shows how abrupt or smooth an image changes in each analyzed voxel, and a specific point represents an edge in the image as well as the orientation of that edge, i.e. the vector obtained gives us the direction of the largest possible increase (black or white) and the value of that change in direction for each voxel. In fact, it is easier to calculate the module of the gradient (see Eq. (7)) than to interprete its direction. The reason is that using the gradient size, a gray-scale image is generated with the defined boundaries, which helps in separating homogenous regions

$$|\nabla I| = \sqrt{\left(\frac{\partial I}{\partial x}\right)^2 + \left(\frac{\partial I}{\partial y}\right)^2 + \left(\frac{\partial I}{\partial z}\right)^2}. \tag{7}$$

The gradient can be highly sensitive to noise if a smoothing technique is not applied before, so the input images passing through this filter were the images previously smoothed by the anisotropic diffusion filter. In some cases, after improving the boundaries with the gradient calculation, an additional filter was applied to strengthen the boundaries and to ensure a suitable segmentation. The library of sigmoid filter provided by ITK[24] was integrated. It transforms the gray-scale intensity values of the image generating an image I_{sigmoind} with the voxels of the strengthen boundaries and the other voxels of the regions progressively smoothed. This filter is configurated using four parameters as follows:

$$I_{\text{sigmoid}} = (\text{Max} - \text{Min})\frac{1}{\left(1 + e^{-\left(\frac{I-\beta}{\alpha}\right)}\right)} + \text{Min}, \tag{8}$$

Biomed. Eng. Appl. Basis Commun. 2014.26. Downloaded from www.worldscientific.com
by Eduardo Soudah on 02/18/15. For personal use only.

Biomed. Eng. Appl. Basis Commun. 2014.26. Downloaded from www.worldscientific.com
by Eduardo Soudah on 02/18/15. For personal use only.

where I contains the input voxels intensity. The image I_{sigmoid} contains the output voxels intensities, Min and Max are the minimum and maximum values of the output image, α is the width of the input intensity range while β defines the intensity over which the range is centered.

Step 3: Image Segmentation

For the segmentation of structures of interest, hybrid algorithms were applied in a sequential manner, and the technique used depended on the type of tissue. Regardless of the segmentation technique chosen, the results would be affected by the image noise causing holes in the extracted regions and even disconnection. To address this problem, the segmentation was carried out after the image preprocessing step through noise reduction and boundaries enhancement techniques.

Region growing

Region growing is widely used in medical applications to extract body structures and its pathologies. In some studies (see for instance Ref. 26) this algorithm was used in brain ventricle segmentation. In Ref. 6 an extra pulmonary tuberculosis infection was segmented by modifying the region growing algorithm while in Ref. 27 the authors extracted the left ventricle in a CT for further numerical analysis.

This technique was used to extract texture connected regions with similar characteristics. The first step of the algorithm establishes manually one or more seeds (spherical volume) within the region of interest. The next step analyzes the neighbor voxels to the region, calculating the average and the standard deviation σ, adding the pixels of position X whose gray-scale intensity values meets the required condition in Eq. (9):

$$I(X) \in [m - f\sigma, m + f\sigma], \tag{9}$$

where I: image, X: neighbor voxel position analyzed, m: mean, σ: standard deviation, f: multiplying factor. The second step was implemented until no more voxels can be added. Finally, the segmented object was represented by all the elements being accepted during the searching process.

Watershed algorithm

The Watershed algorithm is another approach widely used in image segmentation.[28] Its general concept was introduced in Ref. 29 and it is based on mathematical morphology. In this algorithm the image is seen as a topographic surface with rivers and valleys, where the landscape elevation values are defined by the gray-scale value of each pixel or its gradient size. Based on a 3D reconstruction, the image is divided in regions called catchment basins. For each local minimum, a catch basin comprises all the points whose steepest way ends down to its minimum. Finally, watershed is defined by the border lines that separate one basin from the other. The catch basins are labeled by different gray-scale intensity. For each local minimum, a catchment basin comprises all points whose path of steepest descent terminates at this minimum. In this work, watershed was used for big structures segmentations such as the left ventricle and with a continuous texture as with bone structures. In our algorithm, the input image was the gradient magnitude image *Img* obtained during the preprocessing stage (see Eq. (7)), which is considered as a height function where high values represent the borders presence. The first step eliminates the shallow regions below the threshold minimum value which helped to control the over segmentation. From this point, the algorithm created an initial segmentation allowing to track the fastest decrease of each pixel up to its local minimums. The initial result was passed through a second filter which only considered regions with depths lower than the established maximum depth level. In this way the segmentation was controlled up to the segmentation decrease level (catch basins). The parameters threshold and depth were established within the range $[0, 0, -1.0]$ and arbitrarily chosen. As a result of this function, a first image segmentation (I_w) was obtained comprising various segments connected in a non-related way and labeled with a different gray-scale level as described below:

$$I_w = \bigcup_{i=1}^{n} I_i, I_i \cap I_j = \varphi \quad \forall\, i \neq j. \tag{10}$$

One of the main problems of this technique is the over segmentation of regions caused by the images noise, hence the importance of the preprocessing stage to reduce noise and to enhance the edges. It was necessary to group some of the adjacent segments as per their gray-scale levels of the labeled regions in order to obtain the entire volume. Thus, in some cases the final volumes were obtained through the thresholding process, setting the lower threshold in t_0 and the highest threshold to t_f , where $t_0 \leq I_f \leq t_f$.

Step 4: Resampling

Once the segmentation techniques are applied, the volumes are subjected to a resampling process to correct

possible holes in the regions and to smooth surface overlapping. Morphological dilatation techniques and Gauss filters are used for this task.

Step 5: Exporting Geometric Models Using Computer-Aided-Design (CAD) Formats

Volumes were saved in Visualization Toolkit format (*.vtk)[a] to keep the voxels coordinates and their sizes in directions x, y, z and in the Stereolithography format (*.stl)[b] which stores a triangle mesh over the surfaces to define the object shape. We used GiD[30] and ParaView[c] to visualize surface models and mesh generation. Inventor Autodesk[d] was used to transform solid models and finally, Abaqus[e] was used for model discretization and finite-element analysis (FEA). Test boundary conditions were assigned to different regions of the solid volume of the models.

HARD AND SOFT TISSUE MODELS

The algorithms based on image processing techniques described in Sec. 3 were implemented by following the general flowchart shown in Fig. (5). Both algorithms and the results obtained with the proposed methodology applied to DICOM images[f] to obtain the different soft and hard tissue models (the same that were exported to CAD tools) are presented below.

Flowcharts for Hard Tissue Models

In CT images, bone structures are represented with gray levels higher in contrast than other types of tissues present in these images. For this reason, it is useful to apply thresholding techniques to separate the bone tissue from others. Nevertheless, the use of thresholding may have the disadvantage of generate small disconnected areas into the same structure or outside it, then creating overlapped areas on the bone zones. These characteristics make it necessary to use noise filters before the segmentation and resampling the segmented models using morphological dilation techniques to fill the holes and to smooth the outer layer of bone models.

To apply the methodology with hard tissue models, jaw and spine CT images were used combining watershed and threshold algorithms with other preprocessing and resampling filters.

Jaw and spine modeling

The flowchart displayed in Fig. 6 was used to obtain the jaw and spine models. Each process is described below:

- *Preprocessing*: the images noise was reduced using the filtered noise algorithm of anisotropic diffusion and the borders were detected by calculating the gradient module of the filtered image.
- *Segmentation*: for the segmentation stage, a watershed algorithm was applied in the gradient image obtaining a gray-scale image with uniform regions labeled by a gray-scale intensity, see Sec. 3.3.2. Among the obtained set of regions, a zone of interest was chosen with the threshold technique.
- *Resampling and CAD exportation*: a resampling of this initial geometric model was carried out by using a morphological dilatation with one spherical structural element of radio $3 \times 3 \times 3$ to smooth the overlapping surfaces and fill the possible holes that may arise from the segmentation. This model was saved in readable formats by visualization software.
- *Discretization*: finally, using these tools, test boundary conditions were applied to random zones of the model. The geometric model utility was verified for its discretization with the FEM.

Figure 7 shows the results obtained in jaw CT images in DICOM format, size 192×192 pixeles, voxel spacing $1.5625 \times 1.5625 \times 2.5$ mm. Also, Fig. 8 shows the results obtained for each step using spine CT images in format DICOM, 513 slices, size 512×512 pixels, voxel spacing: $0.782 \times 0.782 \times 1.0$ mm.

The geometric model of a jaw is displayed in Fig. 9. Different types of tissues of the jaw bone are discriminated [Fig. 9(A)]: cortical bone, medullary bone, alveoli

[a] *VTK User's Guide*, 5th edn., Kitware, Inc. 2006.
[b] *Stereolithography Interface Specification*, 3D Systems, Inc. 2010.
[c] *ParaView: Parallel Visualization Application. User's Guide, Version 1.6.*, Kitware, Inc. 2009.
[d] Autodesk Inventor Professional. User's Manual and Guide, 2009.
[e] Abaqus 6.9. ABAQUS/CAE User's Manual, 2009.
[f] National Electrical Manufacturers Association. *DICOM: Digital Imaging and Communications in Medicine*, 2008.

Biomed. Eng. Appl. Basis Commun. 2014.26. Downloaded from www.worldscientific.com by Eduardo Soudah on 02/18/15. For personal use only.

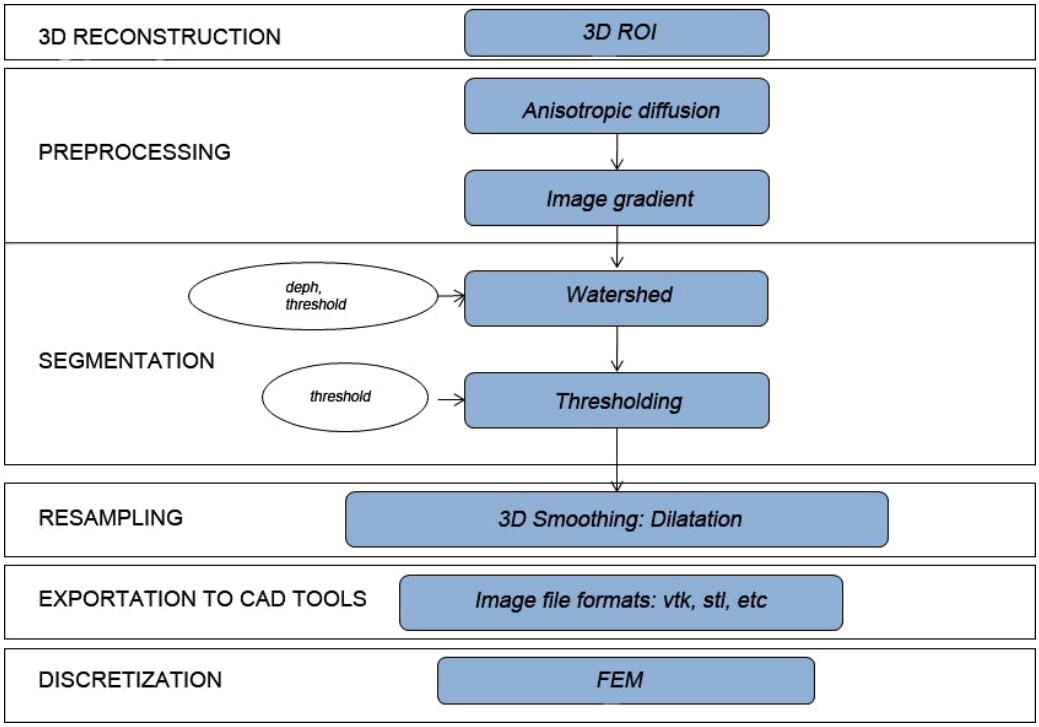

Fig. 6 Flowchart for jaw and spine models.

Biomed. Eng. Appl. Basis Commun. 2014.26. Downloaded from www.worldscientific.com by Eduardo Soudah on 02/18/15. For personal use only.

and even the prosthetic screw implanted to the patient. The surface and mesh views of the volume obtained are presented in Figs. 9(B) and 9(C).

A spine geometric model obtained by the proposed method is presented in Fig. 10. The views presented in this figure have been obtained using the Paraview and GiD softwares.

Flowcharts for Soft Tissue Models

In contrast to the hard tissues, visualization of soft tissue is affected by factors related to its gray values. Intensity variations between different images of soft tissues occur due to the use of different scanners as well as the time of data acquisition. Various contrast enhancements, used to make certain features more prominent, are yet another contribution to the intensity variations across images. Also, some images are affected by the presence of different tissues with similar gray levels and the absence of constant gray levels over the same tissue. On the other hand, soft tissues are characterized by different shape and size, the presence of other body tissue within the target regions or overlaps in medical image, which adds to the complexity of the problem.

The methodology was applied to brain images. To solve the difficulties mentioned above, the task of segmentation was performed using the region growing algorithm, due to its performance when dealing with the intensity and shape variations.

Gray matter modeling

In brain MRI, the brain tissue like other parts of the central nervous system contains white and gray matter, the last the least amount. The segmentation of these structures makes necessary the quantitative morphometric analysis for the diagnosis of various diseases and evaluation of the response to a given treatment. However, the segmentation of brain MRI is affected by the presence of different tissues with similar gray levels and the absence of constant gray levels. Also, medical images of the brain based on MRI and PET, among others, are characterized by noise associated with each type of imaging. The region growing technique can be useful to extract this type of brain tissues due to the flexibility of the method to indicate initial small zones into the desired target tissues through the selection of seeds. Also, it is possible to control and restrict areas that are added in each interaction of the algorithm by defining more sophisticated features as the combination of the mean, standard deviation, entropy, correlation, and other statistical classifiers [see Eq. (9)].

Biomed. Eng. Appl. Basis Commun. 2014.26. Downloaded from www.worldscientific.com
by Eduardo Soudah on 02/18/15. For personal use only.

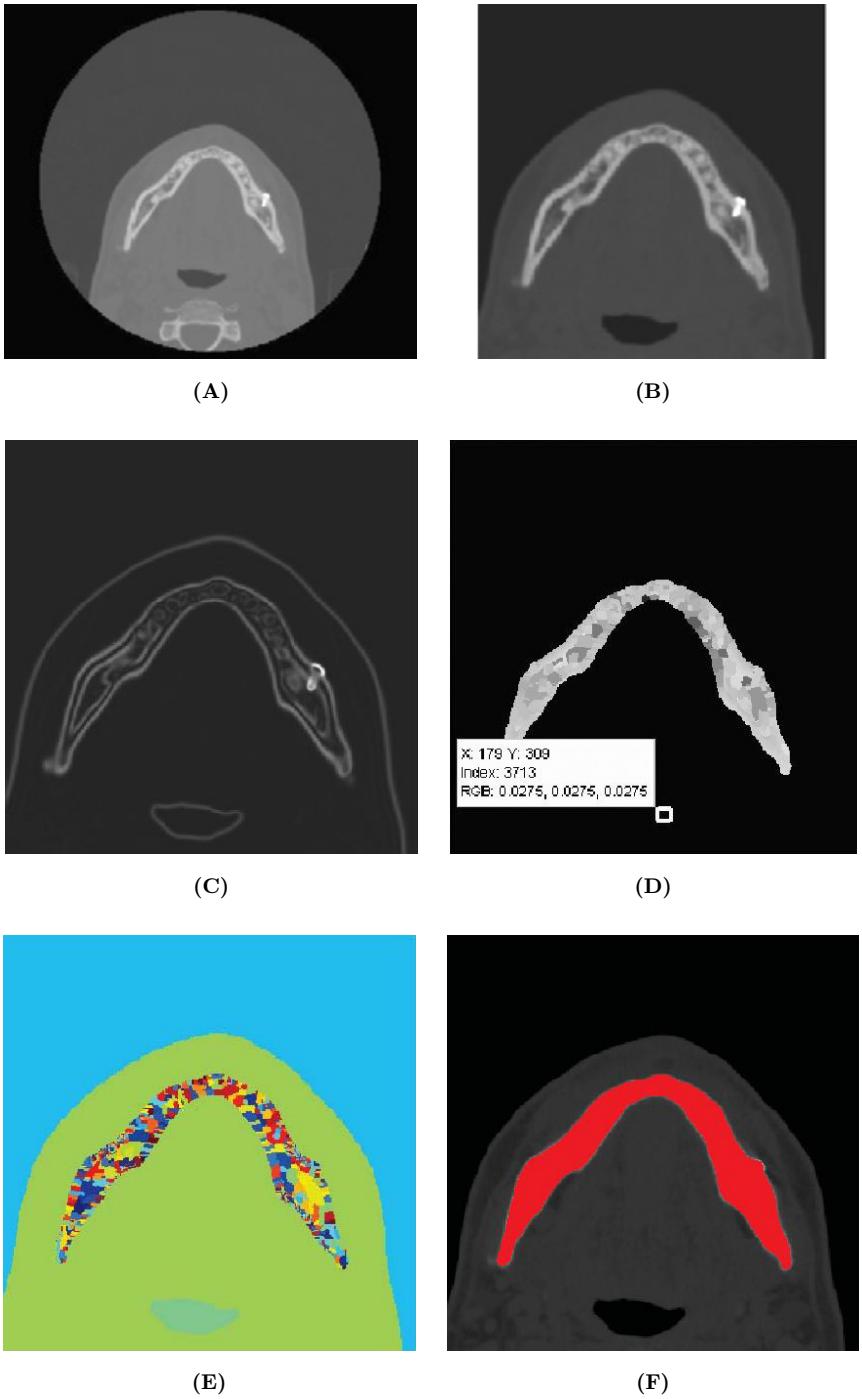

Fig. 7 Jaw bone preproccessing and segmentation. **(A)** CT skull axial slice view. **(B)** ROI with noise reduction through the anisotropic diffusion filter. **(C)** Image Gradient module of B. **(D)** Watershed segmentation applied to border image C. **(E)** Watershed image view on color map. **(F)** Jaw zone selection through threshold technique.

The techniques shown in the flowchart of Fig. 11 were applied to obtain the zone volume of the gray matter geometric model.

- *Preprocessing*: the images noise was filtered using the anisotropic diffusion algorithm smoothing the noise and preserving the images boundaries.
- *Segmentation*: the region growing algorithm was applied over the filtered image, placing spheres (seeds) in the zone of interest. The condition for inclusion is described in Eq. (9) based on the average and the standard deviation of the neighbor voxels (see Sec. 3.3.1). The resulting volume was a binary image with the white material zone colored white (value 255).

Biomed. Eng. Appl. Basis Commun. 2014.26. Downloaded from www.worldscientific.com
by Eduardo Soudah on 02/18/15. For personal use only.

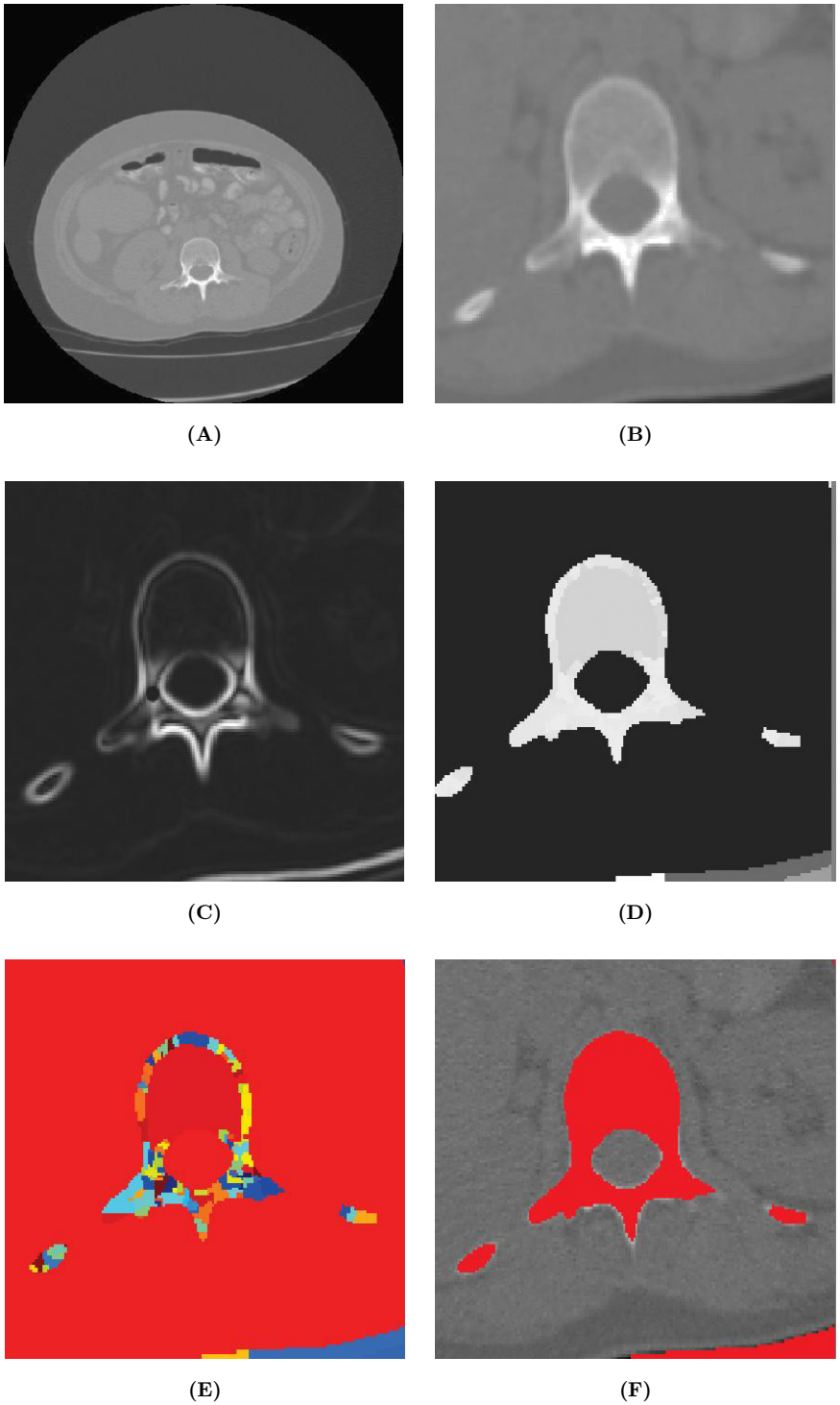

Fig. 8 Preproccessing and segmentation of CT images. **(A)** CT Axial slice view. **(B)** ROI with noise reduction through the anisotropic diffusion filter. **(C)** Image gradient module of B. **(D)** Watershed segmentation applied to border image C. **(E)** Watershed image view on color map. **(F)** Spine zone selection through threshold technique.

- *Resampling and CAD exportation*: in order to improve the initial geometric model, a resampling of the volume was carried out through the morphological dilatation technique with a structural round shaped element of radio $3 \times 3 \times 3$ to smooth the overlapping surfaces and fill the holes generated during the segmentation due to the sensitivity of the segmentation condition. The final geometric model was saved in a

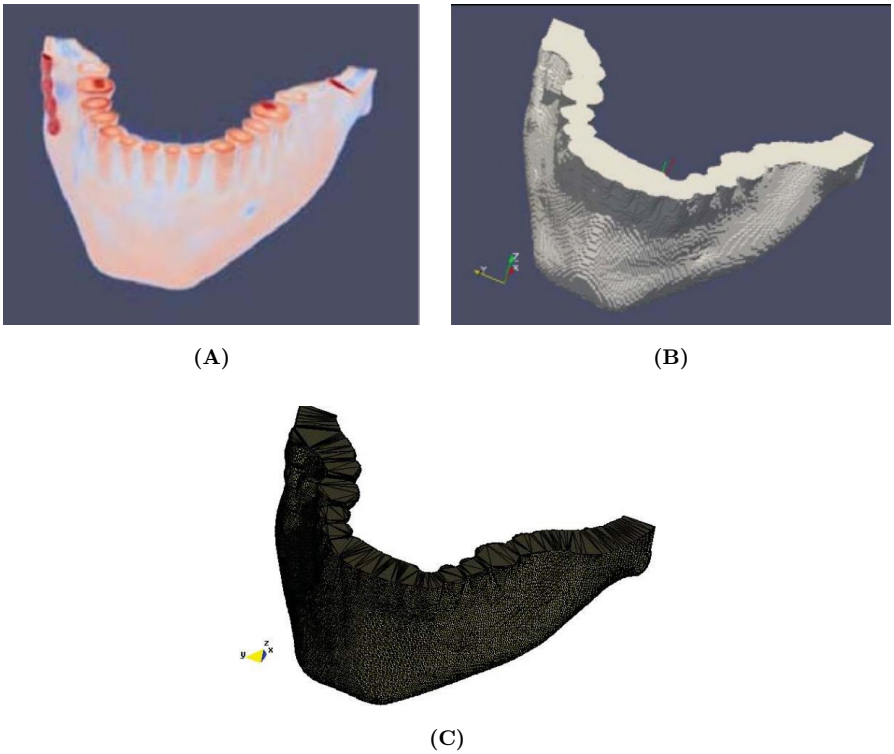

Fig. 9 Jaw volumetric view. **(A)** Jaw bone 3D visualization. **(B)** Surface volume. **(C)** Mesh volume.

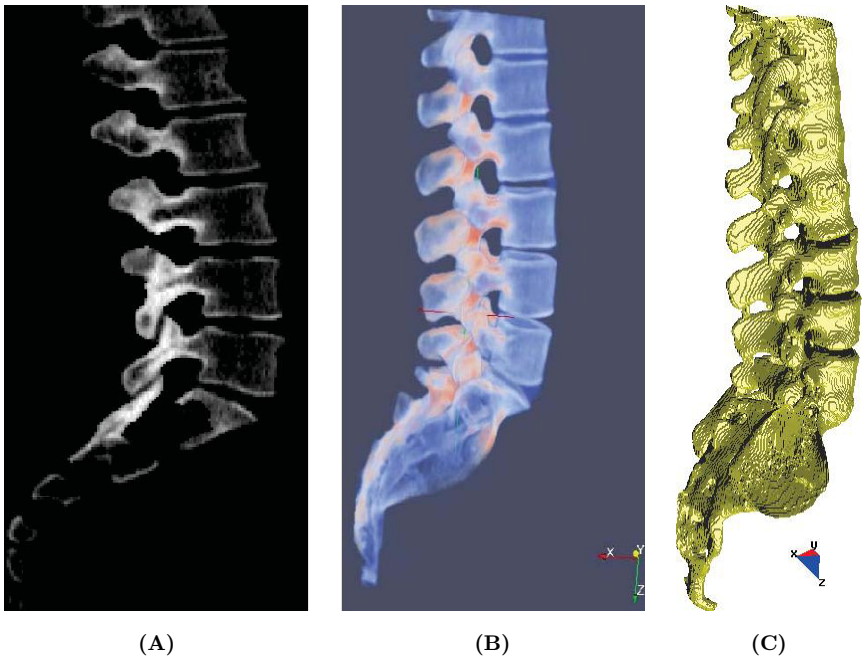

Fig. 10 Views of the spine model. **(A)** Sagittal slice view. **(B)** 3D view using paraview. **(C)** 3D view using GiD.

legible format by a visualization software and CAD tools.

- *Discretization*: finally, using these tools, test boundary conditions were applied over random zones of the model.

Figure 12 displays the results obtained in each stage in brain MRI of DICOM format, 60 slices of sizes 256×256 pixels, voxel spacing: $0.86 \times 0.86\,\text{mm} \times 3.0\,\text{mm}$. For visualization purposes, only one of the axial slices is presented. It can be observed in Fig. 12(B) the selection of

Biomed. Eng. Appl. Basis Commun. 2014.26. Downloaded from www.worldscientific.com
by Eduardo Soudah on 02/18/15. For personal use only.

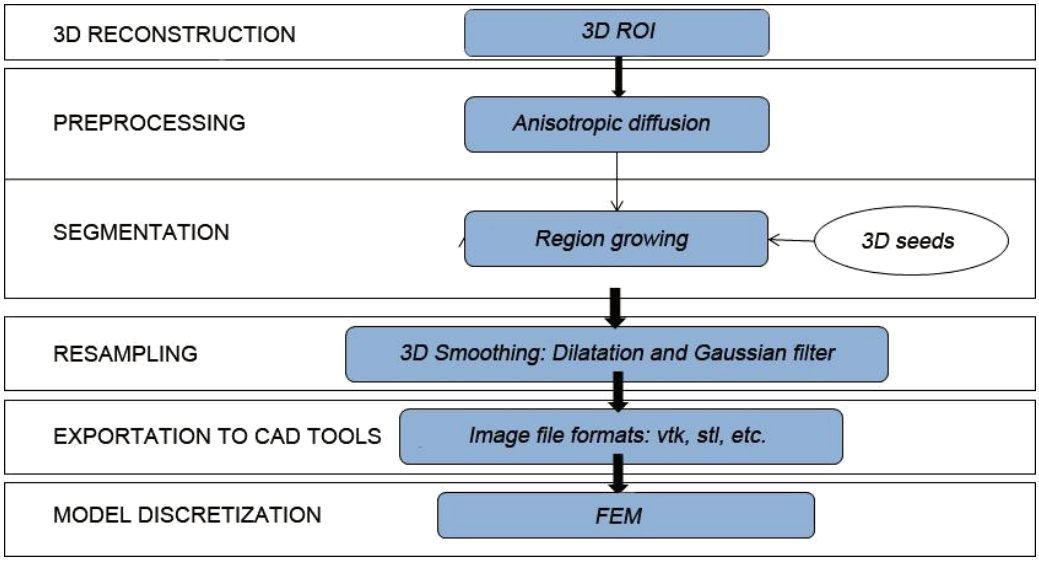

Fig. 11 Flowchart for gray matter model.

Biomed. Eng. Appl. Basis Commun. 2014.26. Downloaded from www.worldscientific.com
by Eduardo Soudah on 02/18/15. For personal use only.

five seeds in the zone of interest. The success of the segmentation will depend on where the seeds are placed.

CPU Processing Time

Through the sequential execution of the proposed preprocessing, segmentation and resampling techniques and following the aforementioned flowcharts, soft and hard tissues geometric models were obtained at very attractive CPU times. The algorithms and libraries used for each study case were developed and integrated into a MATLAB script. In order to perform processing tasks interactively through control buttons and sliders, a graphical user interface (GUI) was developed under the GUI development environment (GUIDE) of MATLAB.

The CPU time required for the five compilations to obtain the three geometric models is presented in Table 1. The computer used was a 64-bits desktop with two processors (Core 2 Quad), 2.66 GHZ speed each one and 8 GB RAM memory.

Validation

Validation experiments are needed to assess the performance of any methodology based on preprocessing and segmentation of medical images. A common approach to validate segmentation methods is through the use of computational phantoms. They simulate the image acquisition process using only simplified models.

The proposed methodology was validated using a computational phantom obtained from brain MRI available in the web site BrainWeb.[13] The flowcharts used were the same applied to obtain de jaw and gray matter models (see Sec. 4.1 and 4.2.1), both based in the region growing and watershed algorithms, respectively. The results were compared to the volumes obtained from web site using statistical texture analysis to quantify the performance of the proposed methodology.

The texture analysis applied to images is related to the spatial distribution of digital levels of the image. For the validation, the texture analysis was applied using statistical descriptors that study the value of the pixel and describe its smoothness, rugosity, etc. Finally, the absolute error percentage of voxels was calculated between both segmented models (segmented and truth models). For consistency purposes only, the statistical descriptors are briefly discussed below:

- *Standard deviation.* It measures the dispersion or contrast among digital levels, being related to the homogeneity observed in the image. In dark images, the standard deviation σ is high if there are high intensity gray level pixels with low gray level background. If $\sigma = 0$, then the image intensity level is constant, if $\sigma = 1$, the image intensity level has high changing values.
- *Skewness.* It measures the histogram's asymmetry. A symmetric histogram will have a third-order moment value close to zero. In mathematical terms, skewness is the asymmetry value of the data with respect to the average. If it is negative, the data is distributed more to the left of the average than to the right. If it is positive, the data is distributed more to the right (or any perfectly symmetric distribution). The μ_3 of a normal distribution is zero. This descriptor is

Biomed. Eng. Appl. Basis Commun. 2014.26. Downloaded from www.worldscientific.com
by Eduardo Soudah on 02/18/15. For personal use only.

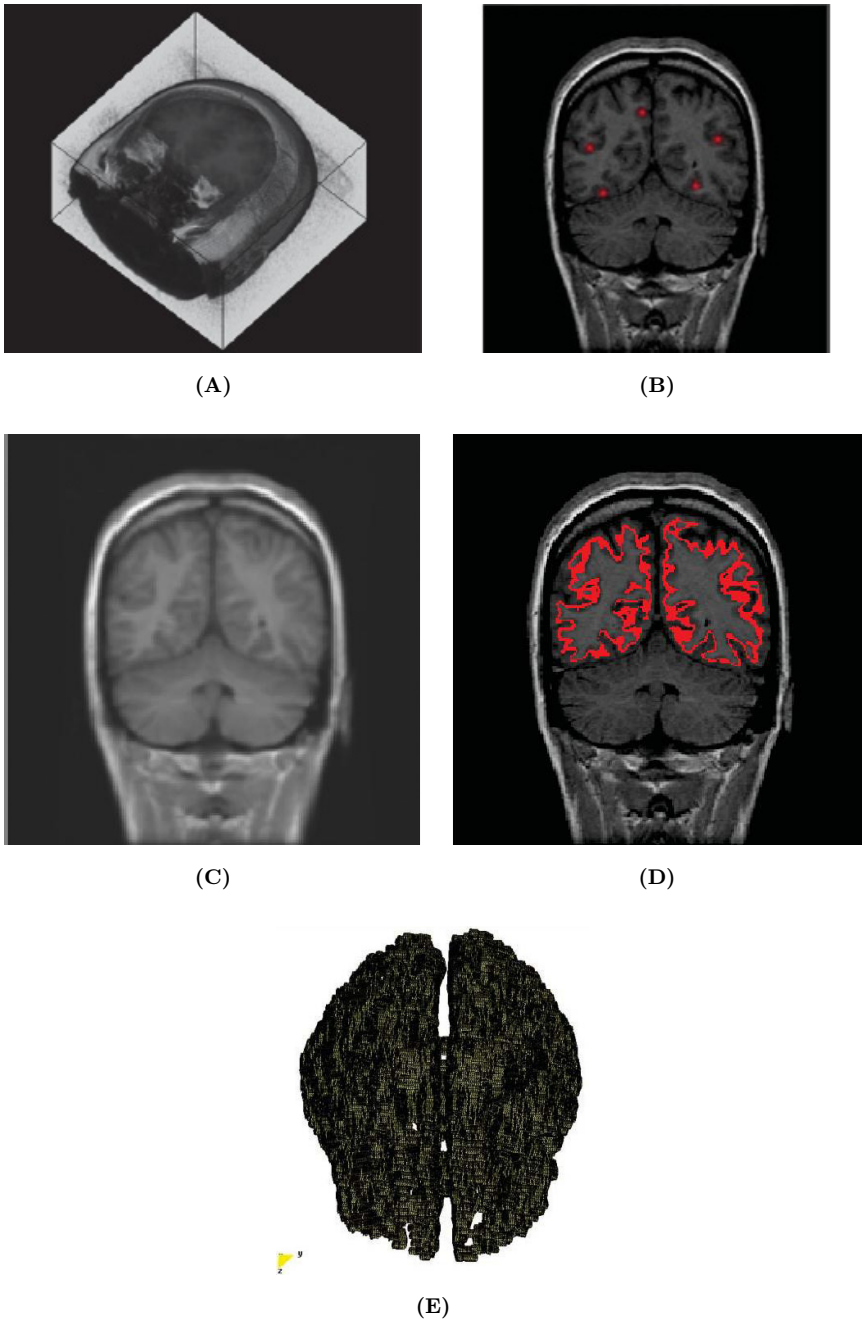

Fig. 12 Segmentation of gray matter using region growing algorithm. **(A)** Original volume from brain MR images. **(B)** Coronal slice view with selection of five initial seeds. **(C)** Denoising of image using anisotropic filter. **(D)** Coronal slice view B with segmented gray material through growing region. **(E)** Volumetric view of the segmented white material in D.

defined as:

$$\mu_3 = \frac{1}{\sigma^3} \sum (i - \mu)^3 h(i), \tag{11}$$

where μ is the mean of gray levels of image, σ is the standard deviation of image, $h(i)$ is the probability histogram for the gray levels.

- *Fourth-order moment (kurtosis).* Kurtosis (μ_4) measures the flattening of the histogram's upper peak. The smaller the value the smoother the peak. The value of a normal distribution is 3. Distributions likely to have more atypical values than the normal distribution have a value greater than 3. Distributions less likely to have atypical values have a value less than 3. Homogeneity of an image is defined as:

$$\mu_4 = \frac{1}{\sigma^4} \sum (i - \mu)^4 h(i), \tag{12}$$

Biomed. Eng. Appl. Basis Commun. 2014.26. Downloaded from www.worldscientific.com
by Eduardo Soudah on 02/18/15. For personal use only.

Table 1. Preprocessing and Segmentation CPU Time (s).

Compilation ID	Flowchart Based on Watershed Algorithm		Flowchart Based on Region Growing Algorithm
	Jaw Bone	Spine Bone	Gray Matter
C_1	40.42	0.052	2.68
C_2	39.35	0.058	2.66
C_3	40.65	0.058	2.65
C_4	40.92	0.055	2.69
C_5	40.98	0.056	2.66

where μ is the mean of gray levels of image, σ is the standard deviation of image, $h(i)$ is the probability histogram for the gray levels.

- *Average entropy.* It measures the image granularity. It is a random statistical data used to charaterize the image texture. A high value indicates a thick texture and its value is zero if it is constant. The entropy is then defined as:

$$\text{Ent} = -\sum h(i), \tag{13}$$

where $h(i)$ is a probability histogram for the gray levels.

The phantom of Brainweb was used as "ground truth" with known substance classes which simulates brain MRI through "fuzzy" volumes where each type of tissue is represented. Global discrete anatomic volumes for each type of voxels were labeled with numerical values as follows:

- 0 = background (BG)
- 1 = cephalicmedulla liquid (CL)
- 2 = gray matter (GM)
- 3 = white matter (WM)
- 4 = fat (FA)
- 5 = muscle/skin (MS)
- 6 = skin (SK)
- 7 = skull (SU)
- 8 = glial matter (GL)
- 9 = connective tissue (CT)

Validation of soft tissue models

First, a region growing algorithm was used to segment a gray matter zone of interest. This segmentation algorithm was applied in three ways: (i) to the original complete discreet phantom, (ii) to the discrete phantom with Gaussian additive noise and a subsequent filtering using the average filtering and (iii) to the discrete phantom with Gaussian additive noise and a subsequent filtering with an anisotropic diffusion filter. These segmentation zones were compared to the gray matter zone provided by the Brainweb. For this purpose, the texture analysis was used by calculating the statistical descriptors in both volumes and the respective percentages of error (%) between the two volumes obtained.

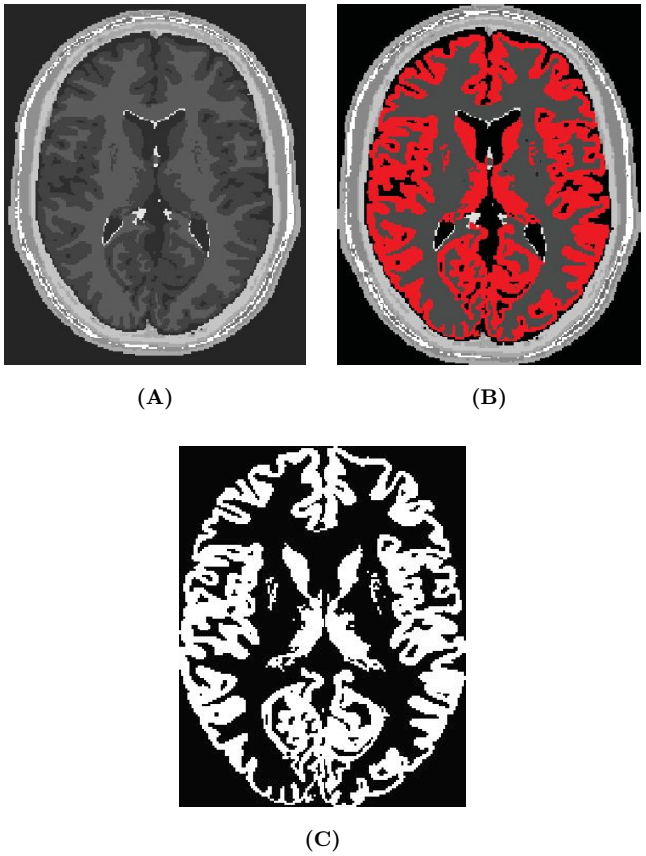

(A) **(B)** **(C)**

Fig. 13 Gray matter segmentation in phantom volume. **(A)** Axial slice number 98 of the original phantom image. **(B)** Gray matter segmentation by the proposed methodology using the region growing algorithm. **(C)** Gray matter zone segmentation by Brainweb.

Figure 13 shows the results obtained during the gray matter zone segmentation in the phantom volume with dimensions $181 \times 217 \times 181$ in directions x, y, z with isotropic voxels of $1.0\,\text{mm}^3$. For visualization purposes, the figure shows only the results corresponding to phantom's 98th slice. Figure 13(B) shows the segmentation zone using the region growing algorithm from four seed points. These points were chosen by the user according to the zone of interest. Spheres of 2-mm radius were used. The coordinates (X, Y, Z) of their centers are: Seed1 = (116, 100, 99), Seed2 = (113, 82, 99), Seed3 = (91, 64, 60), Seed4 = (83, 111, 60). Figure 13(C) shows the gray matter zone provided by the Brainweb.

The texture analysis was carried out to validate the segmentation results by calculating statistical descriptors in the volumes obtained in the gray matter zone. Table 2 collects the statistical values and their

Table 2. Validation of the Volume of the Gray Matter Zone Using the Region-Growing Algorithm and the Statistical Texture Analysis.

	# Pixels	Mean	Stand. Dev.	Asymmetry	Kurtosis	Entropy
Region growing	901195	0.1268	0.3327	2.2436	6.0337	0.5485
Phantom Brainweb	902912	0.1270	0.3330	2.2403	6.0191	0.5492
Error (%)	0.1902	0.1902	0.0813	0.1462	0.2440	0.1224

respective percentage of error, showing that the error in the statistical calculation in segmentation zones is less than 0.3%.

Figure 14 shows the results obtained by segmenting the gray matter in the phantom volumen with additive Gaussian noise and its filtering using the anisotropic diffusion filter following the flowchart of Fig. 11. In Fig. 14(A), the original phantom image is presented showing the axial slice number 98 of the phantom. Figure 14(B) shows the phantom image with Gaussian additive noise. Figure 14(C) shows the resulting image after filtering (B) with the anisotropic diffusion filter-parameters: interacting number = 7, time step = 0.0625 and conductance = 5.0. Also two seeds are observed (seed points) chosen to start the region growing segmentation. The seeds used were spherical with two pixels of radio 2 mm, with the center coordinates X, Y, Z, the seeds coordinates are: Seed1 = (99, 50, 99), Seed2 = (74, 124, 99). Figure 14(D) contains the segmenting results. In Fig. 14(E) the gray matter zone provided by the Brainweb is displayed.

Statistical values were calculated. Their respective percentages of error between the segmented volume and the volume provided by the Brainweb are presented in Table 3. Note that the percentage of error of the statistical calculation in both volumes is less than 7%.

Validation of hard tissue models

Segmenting with the proposed watershed algorithms was also validated using a brain phantom mapped from MRI. Figure 15 displays the results obtained after the graymatter zone segmentation in the phantom volume with dimensions $181 \times 217 \times 181$ (X, Y, Z), with isotropic voxels of $1.0\,\text{mm}^3$. Axial slice number 98 of the original image is presented for visualization purposes in Fig. 15(A). Figure 15(B) shows the segmentation obtained through the watershed algorithm, following the set of preprocessing and segmentation techniques mentioned in flowchart of Fig. 6. The gray matter zone provided by the BrainWeb is presented in Fig. 15(C).

The texture analysis was used to validate the results by calculating statistical descriptors in the obtained

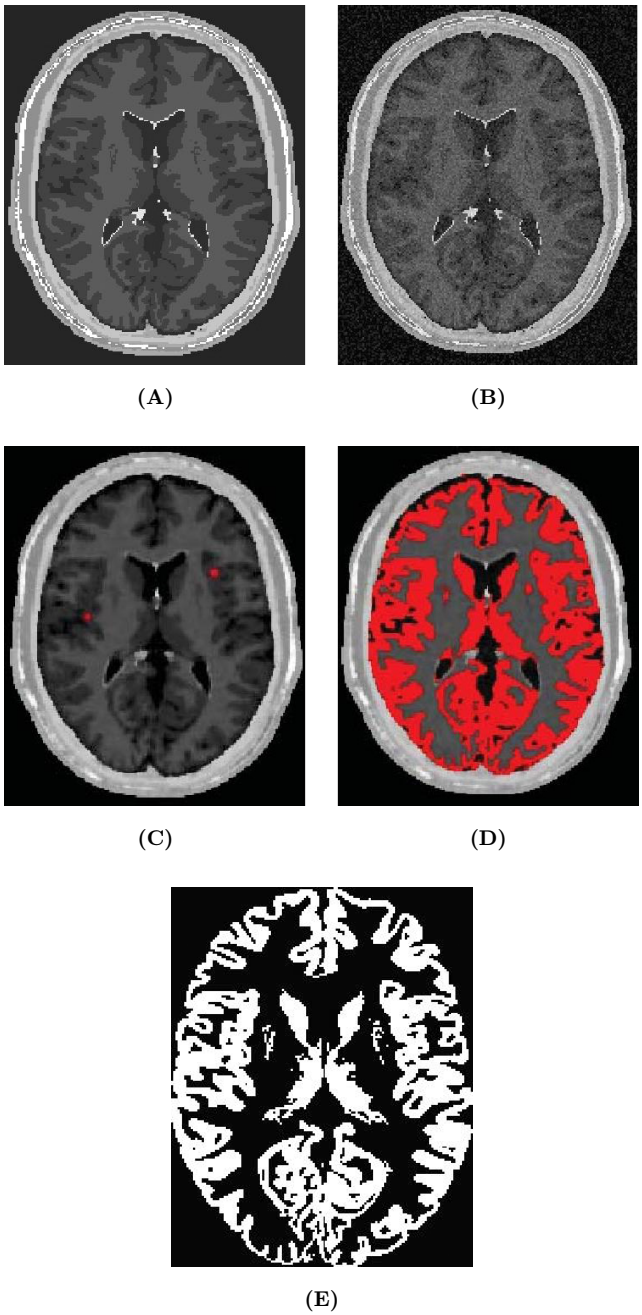

Fig. 14 The segmented gray matter in phantom volume. **(A)** Axial slice number 98 of the original phantom image. **(B)** Original image of the added Gaussian noise. **(C)** Image with noise filtered with an anisotropic diffusion filter and two seeds points. **(D)** Gray matter segmented by the region growing algorithm with five spherical seeds. **(E)** Gray matter zone segmented by Brainweb.

Biomed. Eng. Appl. Basis Commun. 2014.26. Downloaded from www.worldscientific.com by Eduardo Soudah on 02/18/15. For personal use only.

Table 3. Validation of Gray Matter Volume Obtained with Region Growing Algorithm After Adding Gaussian-Noise in a Brain Phantom and Applying the Anisotropic Diffusion-Filter.

	#Pixels	Mean	Stand.Dev.	Asymmetry	Kurtosis	Entropy
Diffusion filter and region growing	955876	0.1345	0.3411	2.1430	5.5926	0.5695
Phantom Brainweb	902912	0.1270	0.3330	2.2403	6.0191	0.5492
Error (%)	5.8659	5.8659	2.4512	4.3421	7.0843	3.7081

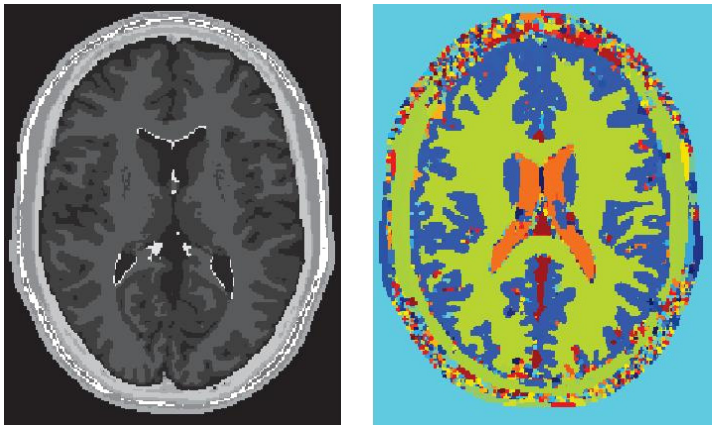

(A) **(B)**

(C) **(D)**

Fig. 15 Gray matter segmentation in brain phantom. **(A)** Axial slice number 98 of an original phantom image. **(B)** and **(C)** Gray matter segmentation through the proposed methodology using the watershed algorithm. **(D)** Gray matter zone segmentated by the BrainWeb.

Table 4. Gray Matter Volumen Validation through Watershed Algorithm.

	# Pixels	Mean	Stand. Dev.	Asymmetry	Kurtosis	Entropy
Diffusion filter and watershed	857718	0.1207	0.3257	2.3293	6.4256	0.5312
Phantom Brainweb	902912	0.1270	0.3330	2.2403	6.0191	0.5492
Error (%)	5.0054	5.0054	2.1806	3.9715	6.7550	3.2679

Biomed. Eng. Appl. Basis Commun. 2014.26. Downloaded from www.worldscientific.com
by Eduardo Soudah on 02/18/15. For personal use only.

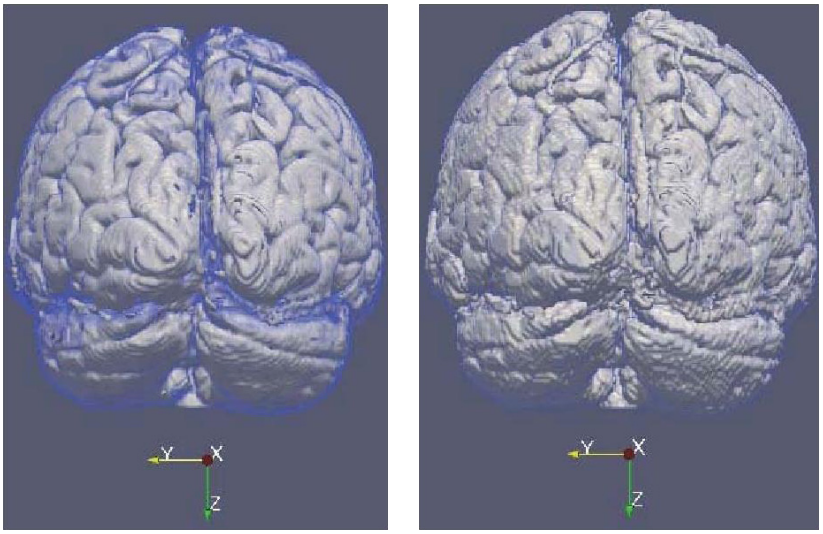

(A) **(B)**

Fig. 16 Volumetric view of the gray matter zone. **(A)** Original volumen of the gray matter provided by the Brainweb. **(B)** Volume obtained by region growing.

Biomed. Eng. Appl. Basis Commun. 2014.26. Downloaded from www.worldscientific.com by Eduardo Soudah on 02/18/15. For personal use only.

volumes. In Table 4 the statistical values and their respective percentage of error are presented. Note that the percentage of error of the statistical calculations in both volumes is less than 2%.

The 3D views of the gray matter zone volume provided by the Brainweb and our methodology are displayed in Fig. 16.

CONCLUDING REMARKS AND FUTURE WORK

One of the main advantages of the proposed approach is that it includes a set of preprocessing and segmentation algorithms that can be combined to create hybrids techniques, which can also adapt themselves to the anatomic structures under study and formulate new flowcharts. The input parameters of the implemented algorithms can be easily calibrated, according to the expert opinions, the observation of tissue type, its intensity profiles and its boundary quality. The computational cost to obtain the tissue models was also attractive and competitive (see Table 1). Also, the results obtained using the proposed methodology are in good agreement when comparing the obtained models against the validated models provided by the Brainweb. The statistical values difference of both volumes was very small. In critical conditions, when corrupting the images with Gaussian-noise (see Table 3), low percentages of error were obtained: number of pixels error = 5.9, average error = 5.9, standard deviation error = 2.5, asymmetry error = 4.3, homogeneity error = 7.1 and entropy error = 3.7. Likewise, it was verified that the implemented techniques are suitable to generate and export volumes in formats *.vtk y *.stl, easy to read from other programs and CAD tools. Their usefulness to generate different meshes, solids and surfaces views was also demonstrated. As for CAD tools, test values were applied in boundary conditions and models were discretized using the FEM, showing the usefulness of the generated volumes for their further numerical analysis.

It should be remarked herein that the current implementation of the proposed approach has some limitations. First, the methodology is demonstrated using only MRI and CT images, other medical images modalities such as PET, 4D MRI could be used. Also, there exist other more sophisticated image-processing algorithms which could be integrated into the methodology.

Finally, the methodology is independent of the underlying properties of the FEM. We only use the morphological operators and Gaussian-filters to smooth the surfaces of tissue models, but other techniques could be applied in order to reduce the mathematical complexity of the soft and hard tissue models and the size and irregularity of the FE mesh as well.

REFERENCES

1. Peterlik I, Sedef M, Basdogan C, Matyska L, Medical imaging analysis of the three dimensional (3D) architecture of trabecular bone: Techniques and their applications, *Comput Graphics* **34**(1):43–54, 2010.

Biomed. Eng. Appl. Basis Commun. 2014.26. Downloaded from www.worldscientific.com by Eduardo Soudah on 02/18/15. For personal use only.

2. Bankman I, *Handbook of Medical Imaging, Processing and Analysis*, Academic Press, UK, 2000.
3. Preim B, Bartz D, *Visualization in Medicine. Theory, Algorithms, and Applications*, Morgan Kaufmann Publishers, Elsevier, NY, 2007.
4. Semmlow J, *Biosignal and Biomedical Image Processing, MATLAB Based Applications*, CRC Press, Boca Raton, 2004.
5. Müller-Karger CM, Rank E, Cerrolaza M, P-version of the finite element method for highly heterogeneous simulation of human bone, *Finite Elem Anal Design* **40**(7):757–770, 2004.
6. Pattijn V, Gelaude F, Vander J, Van R, Medical image-based preformed titanium membranes for bone reconstruction, in Leondes CT, (ed.), *Medical Imaging Systems Technology, Methods in General Anatomy*, Vol. 5, World Scientific Publishing Co. Pte. Ltd., Singapore, 2005.
7. Isaza J, Correa S, Congote J, Methodology for 3D reconstruction of craniofacial structures and their use in the finite element method (in spanish), in *IV Latin American Congress on Biomedical Engineering 2007, Bioengineering Solutions for Latin America Health*, Vol. 18, Springer Berlin, pp. 766–769, 2007.
8. MathWorks, *Image Processing Toolbox TM 6 User's Guide. Release 2009a.* MAT-LAB: Matrix Laboratory, 2009.
9. Acharya T, Ray AK, *Image Processing. Principles and Applications*, John Wiley, NY, 2005.
10. Chuang C-L, Chen C-M, A novel region-based approach for extracting brain tumor in CT images with precision, in Magjarevic R, Nagel JH, Magjarevic R, (eds.), *World Congress on Medical Physics and Biomedical Engineering 2006, IFMBE Proceedings*, Vol. 14, Springer Berlin Heidelberg, pp. 2488–2492, 2007.
11. Avazpour I, Saripan MI, Nordin AJ, Abdullah RSAR, Segmentation of extrapulmonary tuberculosis infection using modified automatic seeded region growing, *Biol Procedures Online* **11**(1):241–252, 2009.
12. Ciofolo C, Fradkin M, Segmentation of pathologic hearts in long-axis late-enhancement MRI, *Med Image Comput Comput Assist Interv* **11**:186–193, 2008.
13. Cocosco C, Kollokian V, Kwan R-S, Evans A, Brainweb: online interface to a 3D MRI simulated brain database, *NeuroImage* **5**(4):S425, 1997.
14. Landini L, Positano V, Santarelli M, 3D medical image processing, in E. Neri, D. Caramella, C. Bartolozzi, (eds.), *Image Processing in Radiology*, Springer, pp. 67–85, 2008.
15. Park H, Kwon M, Han Y, Techniques in image segmentation and 3D visualization in brain MRI and their applications, in Leondes CT, (ed.), *Medical Imaging Systems Technology — Methods in Cardiovascular and Brain Systems*, Vol. 5, World Scientific Publishing Co. Pte. Ltd., Singapore, pp. 207–253, 2005.
16. Goldenberg R, Kimmel R, Rivlin E, Rudzsky M, Techniques in automatic cortical gray matter segmentation of three-dimensional (3D) brain images, in Leondes CT, (ed.), *Medical Imaging Systems Technology — Methods in Cardiovascular and Brain Systems*, Vol. 5, World Scientific Publishing Co. Pte. Ltd., Singapore, 2005.
17. Liew AW-CA, Yan H, Computer techniques for the automatic segmentation of 3D MR brain images, In Leondes CT, (ed.), *Medical Imaging Systems Technology — Methods in Cardiovascular and Brain Systems*, Vol. 5. World Scientific Publishing Co. Pte. Ltd., Singapore, 2005.
18. Peitgen H-O, Oeltze S, Preim B, Geometrical and structural analysis of vessel systems in 3D medical image datasets, in Leondes CT, (ed.), *Medical Imaging Systems Technology — Methods in Cardiovascular and Brain systems*, Vol. 5, World Scientific Publishing Co. Pte. Ltd., Singapore, pp. 1–60, 2005.
19. Accardo AP, Strolka I, Toffanin R, Vittur F, Medical imaging analysis of the three dimensional (3D) architecture of trabecular bone: Techniques and their applications, *Med Imaging Syst Technol, Meth Diagnosis Optimiz* **5**:1–41, 2005.
20. Levoy M, Volume rendering: Display of surfaces from volume data, *IEEE Comput Graphics Appl* **8**(3):29–37, 1988.
21. Lorensen WE, Cline HE, Marching cubes: A high resolution 3D surface construction algorithm, *Comput Graphics* **21**(4):163–169, 1987.
22. Gavidia G, Soudah E, Suit J, Cerrolaza M, Onate E, Development of a Matlab tool to medical image processing and its integration into medical GID software, Technical Report IT-595, CIMNE, International Center of Numerical Methods in Engineering, Barcelona, Spain, 2009.
23. Gavidia G, Soudah E, Martin-Landrove M, Cerrolaza M, Discrete modeling of human body using preprocessing and segmentation techniques of medical images, *Rev. Int'l Met Num Analy Des Eng (in Spanish)* **27**(3):220–226, 2011.
24. Ibáñez L, Schroeder W, Ng L, Cates J, *The ITK Software Guide*, 2nd edn., Kitware Inc, NY, 2005.
25. Perona P, Malik J, Scale-space and edge detection using anisotropic diffusion, *IEEE Trans. Pattern Anal Mach Intell* **12**:629–639, 1990.
26. Liu J, Huang S, Nowinski W, Automatic segmentation of the human brain ventricles from MR images by knowledge-based region growing and trimming, *Neuroinformatics* **7**(2):131–146, 2009.
27. Mühlenbruch G, Das M, Hohl C, Wildberger JE, Rinck D, Flohr T, Koos R, Knackstedt C, Gunther RW, Mahnken AH, Global left ventricular function in cardiac CT evaluation of an automated 3D region-growing segmentation algorithm, *Eur Radiol* **16**(5):1117–1123, 2005.
28. Hahn HK, Peitgen H-O, IWT —interactive watershed transform: A hierarchical method for efficient interactive and automated segmentation of multidimensional gray-scale images, *SPIE Med Imaging* **5032**:643–653, 2003.
29. Digabel H, Lantuejoul C, Iterative algorithms, *Proc 2nd European Symp Quantitative analysis of microstructures*, Vol. 1, Riederer Verlag, pp. 85–99, 1978.
30. Ribó R, Pasenau M, Escolano E, Pérez J, Coll A, Melendo A, *GiD The Personal Pre and Postprocessor. Reference Manual, Version 9*, Internal report, CIMNE, International Center for Numerical Methods in Engineering, Barcelona, 2009.